

WEAK SINDY: A DATA-DRIVEN GALERKIN METHOD FOR SYSTEM IDENTIFICATION

DANIEL A. MESSENGER, DAVID M. BORTZ

ABSTRACT. We present a weak formulation and discretization of the system discovery problem from noisy measurement data. This method of learning differential equations from data fits into a new class of algorithms that replace pointwise derivative approximations with linear transformations and subsequent variance reduction techniques and improves on the standard SINDy algorithm presented in [1] by orders of magnitude. We first show that in the noise-free regime, this so-called Weak SINDy framework is capable of recovering the dynamic coefficients to very high accuracy, with the number of significant digits equal to the tolerance of the data simulation scheme. Next we show that the weak form naturally accounts for measurement noise and recovers approximately twice the significant digits of the standard SINDy algorithm while significantly reducing the size of linear systems in the algorithm. In doing so, we combine the ease of implementation of the SINDy algorithm with the natural noise-reduction of integration as demonstrated in [6] to arrive at a more robust and user-friendly method of sparse recovery that correctly identifies systems in both small-noise and large-noise regimes.

Keywords: data-driven model selection, nonlinear dynamics, sparse recovery, generalized least squares, Galerkin method, adaptive grid, large noise

1. PROBLEM STATEMENT

Consider a dynamical system in D dimensions of the form

$$\frac{d}{dt} \mathbf{x}(t) = \mathbf{F}(\mathbf{x}(t)), \quad \mathbf{x}(0) = \mathbf{x}_0 \in \mathbb{R}^D, \quad 0 \leq t \leq T, \quad (1.1)$$

and measurement data $\mathbf{y} \in \mathbb{R}^{M \times D}$ given at M timepoints $\mathbf{t} = [t_1, \dots, t_M]$ by

$$\mathbf{y}_{md} = \mathbf{x}_d(t_m) + \epsilon_{md}, \quad 1 \leq m \leq M, \quad 1 \leq d \leq D$$

The matrix $\epsilon \in \mathbb{R}^{M \times D}$ represents i.i.d. measurement noise. The focus of this article is the reconstruction of the dynamics (1.1) from the measurements \mathbf{y} .

The SINDy algorithm (Sparse Identification of Non-linear Dynamics [1]) has been shown to be successful in solving this problem for sparsely represented nonlinear dynamics when noise is small and dynamic scales do not vary across multiple orders of magnitude. This framework assumes that the function $\mathbf{F} : \mathbb{R}^D \rightarrow \mathbb{R}^D$ in (1.1) is given component-wise by

$$\mathbf{F}_d(\mathbf{x}(t)) = \sum_{j=1}^J \mathbf{w}_{jd}^* f_j(\mathbf{x}(t)) \quad (1.2)$$

for some known family of functions $(f_j)_{j \in [J]}$ and a sparse weight matrix $\mathbf{w}^* \in \mathbb{R}^{J \times D}$. Here and throughout we define $[N] := \{1, \dots, N\}$. The problem is then transformed into solving for \mathbf{w}^* by building a data matrix

$\Theta(\mathbf{y}) \in \mathbb{R}^{M \times J}$ given by

$$\Theta(\mathbf{y})_{mj} = f_j(\mathbf{y}_m), \quad \mathbf{y}_m = (\mathbf{y}_{m1}, \dots, \mathbf{y}_{mD}),$$

so that the candidate functions are directly evaluated at the noisy data. Solving (1.1) for \mathbf{F} then reduces to solving

$$\dot{\mathbf{y}} = \Theta(\mathbf{y}) \mathbf{w} \quad (1.3)$$

for a sparse weight matrix \mathbf{w} , where $\dot{\mathbf{y}}$ is the numerical time derivative of \mathbf{y} . Sequentially-thresholded least squares is then used to arrive at a sparse solution.

The formulation of system discovery problems in terms of a candidate basis of nonlinear functions (1.2) and subsequent discretization (1.3) was first introduced in [7] in the context of catastrophe prediction with compressed sensing techniques used to enforce sparsity. Since then there has been an explosion of interest in the problem of identifying nonlinear dynamical systems from data, with some of the primary techniques being Gaussian process regression, deep neural networks ([5]), Bayesian inference ([9], [10]) and a variety of methods from numerical analysis ([2], [3]). These techniques have been successfully applied to discovery of both ordinary and partial differential equations. The variety of approaches qualitatively differ in the interpretability of the resulting data-driven dynamical system, the practicality of the algorithm, and the robustness due to noise, scale separation, and so on. For instance, a neural-network based data-driven dynamical system does not easily lend itself to physical interpretation. As well, certain sparsification techniques are not practical to the general scientific community, where the problem of system identification from data is ubiquitous. The SINDy algorithm allows for direct interpretations of the dynamics from identified differential equations and uses sequentially thresholded least-squares to enforce sparsity, which is not nearly as robust as other approaches but is easy to implement and has been proven to converge to sparse local minimizers in [8]. For these reasons, we use sequential thresholding in this article to demonstrate the viability of the method, and note that improvement using a more robust sparsifying strategy is possible.

The aim of the present article is to provide rigorous justification for using the weak formulation of the dynamics in place of local point-wise derivative approximations, as well as a robust algorithm for doing so. As such, we restrict numerical experiments to autonomous ordinary differential equations for their immenability to analysis. In future works, more robust sparsification measures will be explored. As well, adaptation to PDEs and non-autonomous systems is forthcoming. We note that the use of integral equations for system identification was introduced in [6], where compressed sensing techniques were used to enforce sparsity, and that this technique can be seen as a special case of the method introduced here. In section 2 we introduce the algorithm with analysis of the resulting error structure and in section 3 we provide numerical experimentation with a range of nonlinear systems.

2. WEAK SINDY

In this article, we approach the problem (1.3) from a different perspective, by utilizing the weak form of the differential equation. Recall that for any smooth test function $\phi : \mathbb{R} \rightarrow \mathbb{R}$ (absolutely continuous is

enough) and interval $(a, b) \subset [0, T]$, equation (1.1) admits the weak formulation

$$\phi(b)\mathbf{x}(b) - \phi(a)\mathbf{x}(a) - \int_a^b \phi'(u) \mathbf{x}(u) du = \int_a^b \phi(u) \mathbf{F}(\mathbf{x}(u)) du, \quad 0 \leq a < b \leq T. \quad (2.1)$$

With $\phi = 1$, we arrive at the integral equation of the dynamics explored in [6]. If we instead take ϕ to be non-constant and compactly supported in (a, b) , we arrive at

$$- \int_a^b \phi'(u) \mathbf{x}(u) du = \int_a^b \phi(u) \mathbf{F}(\mathbf{x}(u)) du. \quad (2.2)$$

We then define the generalized residual $\mathcal{R}(\mathbf{w}; \phi)$ for a given test function by replacing \mathbf{F} with a candidate element from the span of $(f_j)_{j \in [J]}$ and \mathbf{x} with \mathbf{y} as follows:

$$\mathcal{R}(\mathbf{w}; \phi) := \int_a^b \left(\phi'(u) \mathbf{y}(u) + \phi(u) \left(\sum_{j=1}^J \mathbf{w}_j f_j(\mathbf{y}(u)) \right) \right) du. \quad (2.3)$$

Clearly with $\mathbf{w} = \mathbf{w}^*$ and $\mathbf{y} = \mathbf{x}(t)$ we have $\mathcal{R}(\mathbf{w}; \phi) = 0$ for all ϕ compactly-supported in (a, b) ; however, \mathbf{y} is a discrete set of data, hence (2.3) can at best be approximated numerically, with measurement noise presenting a significant barely to accurate quadrature.

2.1. Method Overview. For analogy with traditional Galerkin methods, consider the forward problem of solving a dynamical system such as (1.1) for \mathbf{x} . The Galerkin approach is to seek a solution \mathbf{x} represented in a chosen trial basis $(f_j)_{j \in [J]}$ such that the residual \mathcal{R} , defined by

$$\mathcal{R} = \int \phi(t)(\dot{\mathbf{x}}(t) - \mathbf{F}(\mathbf{x}(t))) dt,$$

is minimized over all test functions ϕ living in the span of a given test function basis $(\phi_k)_{k \in [K]}$. If the trial and test function bases are known analytically, inner product of the form $\langle f_j, \phi_k \rangle$ appearing in the residual can be computed exactly, so that computational errors result only from representing the solution in a finite-dimensional function space.

The method we present here can be considered a data-driven Galerkin method of solving for \mathbf{F} where the trial “basis” is given by the set of gridfunctions $(f_j(\mathbf{y}))_{j \in [J]}$ evaluated at the data and only the test-function basis $(\phi_k)_{k \in [K]}$ is known analytically. In this way, inner products appearing in $\mathcal{R}(\mathbf{w}; \phi)$ must be approximated numerically, implying that the accuracy of the recovered weights \mathbf{w} is ultimately limited by the quadrature scheme used to discretize inner products. Using Lemma 2.1 below, we show that the correct coefficients \mathbf{w}^* may be recovered to effective machine precision accuracy (given by the tolerance of the forward ODE solver) from noise-free trajectories \mathbf{y} by discretizing (2.2) using the trapezoidal rule and choosing ϕ to decay smoothly to zero at the boundaries of its support.

Having chosen a quadrature scheme, the next accuracy barrier is presented by measurement noise, which introduces a bias in the weights. Below we analyze the distribution of the residuals $\mathcal{R}(\mathbf{w}; \phi)$ to arrive at a generalized least squares approach where the covariance matrix can be computed directly from the test functions. This analysis also shows that placing test functions near steep gradients in the dynamics improves

recovery, hence we develop a self-consistent and stable algorithm for constructing a test function basis adaptively near these regions which also does not rely on pointwise approximation of derivatives. Overall, we show that when noise is present, our method produces a recovered weight matrix $\hat{\mathbf{w}}$ with the number of significant digits scaling optimally with the signal-to-noise ratio σ_{SNR} (defined below).

Remark. The weak formulation of the dynamics (2.2) introduces a wealth of information. Given M timepoints $\mathbf{t} = (t_m)_{m \in [M]}$, equation (2.2) affords $K = M(M - 1)/2$ residuals over all possible supports $(a, b) \subset \mathbf{t} \times \mathbf{t}$. Using multiple families of test functions $(\{\phi_k^1\}_{k \in [K_1]}, \{\phi_k^2\}_{k \in [K_2]}, \dots)$ over these supports can be viewed as a type of data assimilation, with the action of each test function providing useful information for the covariance structure of the residuals. The information complexity of such an exhaustive approach quickly becomes computationally intractable; however, we show here that even with large noise recovery the true weights \mathbf{w}^* using $K \ll M$.

2.2. Algorithm: Weak SINDy. We state here the Weak SINDy algorithm in full generality, which uses a generalized least squares approach with regularization and sequential thresholding to enforce sparsity.

$\hat{\mathbf{w}} = \text{Weak_SINDy}(\mathbf{y}, \mathbf{t} ; (\phi_k)_{k \in [K]}, (f_j)_{j \in [J]}, \Omega, \lambda, \gamma)$:

- (1) Construct matrix of trial gridfunctions $\Theta(\mathbf{y}) = [f_1(\mathbf{t}, \mathbf{y}) \mid \dots \mid f_J(\mathbf{t}, \mathbf{y})]$
- (2) Construct integration matrices \mathbf{V}, \mathbf{V}' from test functions ϕ_k such that the k th rows satisfy $\mathbf{V}_k = \Delta t \phi_k(\mathbf{t}), \mathbf{V}'_k = \Delta t \phi'_k(\mathbf{t})$
- (3) Compute Gram matrix $\mathbf{G} = \mathbf{V}\Theta(\mathbf{y})$ and right-hand side $\mathbf{b} = -\mathbf{V}'\mathbf{y}$ so that $\mathbf{G}_{kj} = \langle \phi_k, f_j(\mathbf{y}) \rangle$ and $\mathbf{b}_{kd} = -\langle \phi'_k, \mathbf{y}_d \rangle$
- (4) Solve the generalized least-squares problem with ℓ_2 -regularization

$$\hat{\mathbf{w}} = \operatorname{argmin}_{\mathbf{w}} \left\{ (\mathbf{G}\mathbf{w} - \mathbf{b})^T \Omega^{-1} (\mathbf{G}\mathbf{w} - \mathbf{b}) + \gamma^2 \|\mathbf{w}\|_2^2 \right\},$$

using $\text{SINDy}(\lambda)$ to enforce sparsity.

Below we analyze the residual to arrive at near optimal strategies for choosing Ω and $(\phi_k)_{k \in [K]}$ directly from the data (\mathbf{t}, \mathbf{y}) . The choice of test function basis is chosen in tandem with a quadrature rule to eliminate numerical errors. Methods of choosing the sparsity and regularization parameters λ and γ a priori from the data exist [4], however in this article we do not optimize this process in order to focus on errors resulting from the weak formulation of the dynamics.

2.3. Residual Analysis. Performance of the Weak SINDy method is determined by the behavior of the residuals

$$\mathcal{R}_k(\mathbf{w}) = (\mathbf{G}\mathbf{w} - \mathbf{b})_k.$$

Expanding this out and linearizing around the true data, we have

$$\begin{aligned}
(\mathbf{G}\mathbf{w} - \mathbf{b})_k &= \langle \phi_k, \Theta(\mathbf{y})\mathbf{w} \rangle + \langle \phi'_k, \mathbf{y} \rangle \\
&= \langle \phi_k, \Theta(\mathbf{y})(\mathbf{w} - \mathbf{w}^*) \rangle + \langle \phi_k, \Theta(\mathbf{y})\mathbf{w}^* \rangle + \langle \phi'_k, \mathbf{y} \rangle \\
&= \underbrace{\langle \phi_k, \Theta(\mathbf{y})(\mathbf{w} - \mathbf{w}^*) \rangle}_{R_1} + \underbrace{\langle \phi_k, \epsilon \nabla \mathbf{F}(\mathbf{x}) \rangle}_{R_2} + \underbrace{\langle \phi'_k, \epsilon \rangle}_{R_3} + I_k + \mathcal{O}(\epsilon^2)
\end{aligned}$$

where $\nabla F(\mathbf{x})_{id} = \frac{\partial \mathbf{F}_d}{\partial \mathbf{x}_i}(\mathbf{x})$. The errors manifest in the following ways:

- R_1 is the misfit between \mathbf{w} and \mathbf{w}^*
- R_2 results from measurement error in trial gridfunctions $f_j(\mathbf{y}) = f_j(\mathbf{x} + \epsilon)$
- R_3 results from replacing \mathbf{x}_m with $\mathbf{y}_m = \mathbf{x}(t_m) + \epsilon_m$ in the right-hand side of (1.1)
- I_k is the integration error ($\mathcal{O}(\Delta t^{p_k+1})$) by Lemma 2.1)
- $\mathcal{O}(\epsilon^2)$ results from truncating the Taylor expansion of $\mathbf{F}(\mathbf{y})$ around the exact data \mathbf{x} :

$$\mathbf{F}(\mathbf{y}_m) = \mathbf{F}(\mathbf{x}(t_m)) + \epsilon_m \nabla \mathbf{F}(\mathbf{x}(t_m)) + \mathcal{O}(\epsilon_m^2).$$

Clearly, recovery of \mathbf{F} when $\epsilon = 0$ is straight forward: R_1 and I_k are the only error terms, thus one only needs to select a quadrature scheme so that the integration error I_k is negligible $\hat{\mathbf{w}} = \mathbf{w}^*$ will be the minimizer (Figure 2 demonstrates this fact).

For $\epsilon > 0$, accurate recovery of \mathbf{F} requires one to choose hyperparameters that exemplify the true misfit term R_1 by enforcing that the other error terms are of lower order. We look for $(\phi_k)_{k \in [K]}$ and $\Omega = \mathbf{C}\mathbf{C}^T$ that approximately enforce $\mathbf{C}^{-1}\mathcal{R} \sim \mathcal{N}(0, \sigma^2 \mathbf{I})$ utilizing that minimizing the residual in the least-squares sense corresponds to normally-distributed errors.

Approximate Covariance Ω . Neglecting I_k and $\mathcal{O}(\epsilon^2)$, we can rewrite \mathcal{R}_k with R_2 and R_3 together as

$$\mathcal{R}_k(\mathbf{w}) = R_1 + \sum_m \mathbf{z}_m, \quad \mathbf{z}_m = \epsilon_m B_m \Delta t$$

with

$$B_m = \phi'_k(t_m) \mathbf{I}_D + \phi_k(t_m) \nabla \mathbf{F}(\mathbf{x}(t_m)), \quad \epsilon_m = [\epsilon_{1m} \ \epsilon_{2m} \ \dots \ \epsilon_{Dm}],$$

where \mathbf{I}_D is the identity in $\mathbb{R}^{D \times D}$. Assuming ϵ are i.i.d with mean μ and variance σ^2 , the transformed random variables \mathbf{z}_m are also i.i.d. and so the Lyupanov central limit theorem asserts that

$$\mathcal{R}_k \sim \mathcal{N}(R_2, \Sigma_k)$$

with

$$\Sigma_k := \text{cov} \left(\sum_m \epsilon_m B_m \Delta t \right) = \sum_m \text{cov}(\epsilon_m B_m \Delta t) = \Delta t^2 \sigma^2 \sum_m B_m^T B_m.$$

If it holds that $\|\phi'_k\|_\infty \gg \|\phi_k\|_\infty$, then we get

$$\Sigma_k \approx \sigma^2 \left(\Delta t \|\phi'_k\|_2^2 \right) \mathbf{I}_D.$$

If we then consider the entire residual vector \mathcal{R} , this corresponds to the approximate distribution

$$\mathcal{R} \sim \mathcal{N}(R_1, \Omega)$$

with $\Omega = \mathbf{V}'(\mathbf{V}')^T$, or $\Omega_{ij} = \Delta t^2 \sum_{m=1}^M \phi'_i(t_m) \phi'_j(t_m) = \Delta t \langle \phi'_i, \phi'_j \rangle$.

Adaptive Refinement. Before advocating for a particular type of test function basis, we show that by localizing ϕ_k around large $\dot{\mathbf{x}}$, an approximate cancellation of the error terms R_2 and R_3 results. Consider the one-dimensional case ($D = 1$). When $\dot{\mathbf{x}}(t_m)$ is large compared to ϵ , we approximately have

$$\mathbf{y}_m = \mathbf{x}(t_m) + \epsilon_m \approx \mathbf{x}(t_m + \delta t) \approx \mathbf{x}(t_m) + \delta t \mathbf{F}(\mathbf{x}(t_m)) \quad (2.4)$$

for some δt , i.e. the perturbed value \mathbf{y}_m lands close to the true trajectory \mathbf{x} at the time $t_m + \delta t$. Visually this is clear, and for a heuristic argument, let δt be the point of intersection between the tangent line at $\mathbf{x}(t_m)$ and $\mathbf{x}(t_m) + \epsilon$:

$$\mathbf{x}(t_m) + \delta t \dot{\mathbf{x}}(t_m) = \mathbf{x}(t_m) + \epsilon \implies \delta t = \frac{\epsilon}{\dot{\mathbf{x}}(t_m)}.$$

When $\dot{\mathbf{x}}(t_m)$ is large compared to ϵ , such an intersection exists and δt will be very small, hence $\mathbf{x}(t_m) + \epsilon$ will approximately lie on the true trajectory.

If we linearize \mathbf{F} using this approximation we get

$$\mathbf{F}(\mathbf{y}_m) \approx \mathbf{F}(\mathbf{x}(t_m)) + \delta t \mathbf{F}'(\mathbf{x}(t_m)) \mathbf{F}(\mathbf{x}(t_m)) = \mathbf{F}(\mathbf{x}(t_m)) + \delta t \ddot{\mathbf{x}}(t_m). \quad (2.5)$$

Assuming ϕ_k is sufficiently localized around t_m , (2.4) implies that

$$\langle \phi'_k, \mathbf{x} \rangle + \underbrace{\langle \phi'_k, \epsilon \rangle}_{R_3} = \langle \phi'_k, \mathbf{y} \rangle \approx \langle \phi'_k, \mathbf{x} \rangle + \delta t \langle \phi'_k, \mathbf{F}(\mathbf{x}) \rangle,$$

hence $R_3 \approx \delta t \langle \phi'_k, \mathbf{F}(\mathbf{x}) \rangle$, while (2.5) implies

$$\begin{aligned} \langle \phi_k, \Theta(\mathbf{y}) \mathbf{w} \rangle &= \underbrace{\langle \phi_k, \Theta(\mathbf{y})(\mathbf{w} - \mathbf{w}^*) \rangle}_{=R_2} + \langle \phi_k, \mathbf{F}(\mathbf{y}) \rangle \\ &\approx \langle \phi_k, \Theta(\mathbf{y})(\mathbf{w} - \mathbf{w}^*) \rangle + \langle \phi_k, \mathbf{F}(\mathbf{x}) \rangle + \underbrace{\delta t \langle \phi'_k, \ddot{\mathbf{x}} \rangle}_{\approx R_2} \\ &= \langle \phi_k, \Theta(\mathbf{y})(\mathbf{w} - \mathbf{w}^*) \rangle + \langle \phi_k, \mathbf{F}(\mathbf{x}) \rangle - \delta t \langle \phi'_k, \mathbf{F}(\mathbf{x}) \rangle \end{aligned}$$

having integrated by parts. Putting the pieces together, the residual takes the form

$$\mathcal{R}_k(\mathbf{w}) = \langle \phi'_k, \mathbf{y} \rangle + \langle \phi_k, \Theta(\mathbf{y}) \mathbf{w} \rangle \approx R_2,$$

and we see that R_2 and R_3 have effectively canceled. In higher dimensions this interpretation breaks down, but nevertheless, for any given coordinate \mathbf{x}_d , it holds that terms in the error expansion vanish around points t_m where $\dot{\mathbf{x}}_d$ is large, precisely because $\mathbf{x}_d(t_m) + \epsilon \approx \mathbf{x}_d(t_m + \delta t)$.

2.4. Test Function Basis $(\phi_k)_{k \in [K]}$. Here we arrive at a test functions space \mathcal{S} and quadrature scheme to minimize integration errors and enact the heuristic arguments above, which rely on ϕ_k sufficiently localized. To ensure the integration error in approximating inner products $\langle f_j, \phi_k \rangle$ is negligible, we rely on the following lemma, which provides a bound on the error in discretizing the weak derivative relation

$$- \int \phi' f \, dt = \int \phi f' \, dt \quad (2.6)$$

for compactly supported ϕ .

Lemma 2.1 (Numerical Error in Weak Derivatives). *Let f, ϕ have continuous derivatives of order p and define $t_j = a + j \frac{b-a}{N} = a + j\Delta t$. Then if ϕ has roots $\phi(a) = \phi(b) = 0$ of multiplicity p , then*

$$\frac{\Delta t}{2} \sum_{j=0}^{N-1} [g(t_j) + g(t_{j+1})] = \mathcal{O}(\Delta t^{p+1}), \quad (2.7)$$

where $g(t) = \phi'(t)f(t) + \phi(t)f'(t)$. In other words, the composite trapezoidal rule discretizes the weak derivative relation (2.6) to order $p+1$.

Proof. This is a simple consequence of the Euler-Maclaurin formula. If $g : [a, b] \rightarrow \mathbb{C}$ is a smooth function, then

$$\frac{\Delta t}{2} \sum_{j=0}^{N-1} [g(t_j) + g(t_{j+1})] \sim \int_a^b g(t) dt + \sum_{k=1}^{\infty} \frac{\Delta t^{2k} B_{2k}}{(2k)!} (g^{(2k-1)}(b) - g^{(2k-1)}(a)),$$

where B_{2k} are the Bernoulli numbers. The asymptotic expansion provides corrections to the trapezoidal rule that realize machine precision accuracy up until a certain value of k , after which terms in the expansion grow and the series diverges.

In our case, $g(t) = \phi'(t)f(t) + \phi(t)f'(t)$ where the root conditions on ϕ imply that

$$\int_a^b g(t) dt = 0 \quad \text{and} \quad g^{(k)}(b) = g^{(k)}(a) = 0, \quad 0 \leq k \leq p-1.$$

So for p odd, we have that

$$\begin{aligned} \frac{\Delta t}{2} \sum_{j=0}^{N-1} [g(t_j) + g(t_{j+1})] &\sim \sum_{k=(p+1)/2}^{\infty} \frac{\Delta t^{2k} B_{2k}}{(2k)!} (g^{(2k-1)}(b) - g^{(2k-1)}(a)) \\ &= \frac{B_{p+1}}{(p+1)!} (\phi^{(p)}(b)f(b) - \phi^{(p)}(a)f(a)) \Delta t^{p+1} + \mathcal{O}(\Delta t^{p+2}). \end{aligned}$$

For even p , the leading term is $\mathcal{O}(\Delta t^{p+2})$ with a slightly different coefficient. \square

We now define the test functions space \mathcal{S} to be uni-modal piece-wise polynomials of the form

$$\phi(t) = \begin{cases} C(t-a)^p(b-t)^q & t \in (a, b), \\ 0 & \text{otherwise,} \end{cases}$$

where $(a, b) \subset \mathbf{t} \times \mathbf{t}$ satisfies $a < b$ and $p, q \geq 1$. Functions $\phi \in \mathcal{S}$ are compactly supported in $[0, T]$ and non-negative. The normalization

$$C = \frac{1}{p^p q^q} \left(\frac{p+q}{b-a} \right)^{p+q}$$

ensures that $\|\phi\|_{\infty} = 1$. With $p = q$, the exact leading order error in term in (2.7) is

$$\frac{2^p B_{p+1}}{p+1} (f(b) - f(a)) \Delta t^{p+1},$$

which is negligible for a wide range of reasonable p and Δt values. The Bernoulli numbers eventually start growing like p^p , but for smaller values of p they are moderate. For instance, with $\Delta t = 0.1$ and $f(b) - f(a) = 1$, this error term is $o(1)$ up until $p = 85$, where it takes the value 0.495352, while for $\Delta t = 0.01$, the error is below machine precision for all p between 7 and 819. For these reasons, in what follows we choose test functions $(\phi_k)_{k \in [K]} \subset \mathcal{S}$ and discretize all integrals using the trapezoidal rule. Unless otherwise stated,

each function ϕ_k satisfies $p = q$ and so is fully determined by the tuple $\{p_k, a_k, b_k\}$ indicating its polynomial degree and support.

Strategy 1: Uniform Grid. The simplest strategy for choosing a test function basis $(\phi_k)_{k \in [K]} \subset \mathcal{S}$ is to place ϕ_k uniformly on the interval $[0, T]$ each with support size

$$L := \|[a, b] \cap \mathbf{t}\|_0$$

and a polynomial degree p . This is the uniform grid strategy, only in light of the residual analysis above we introduce two parameters ρ and s below to pick the degree p and the number of basis functions K . We fix the support L by

$$L = \frac{1}{2} \left(\frac{M}{\operatorname{argmax}_n |\hat{\mathbf{y}}|_n} \right) \quad (2.8)$$

where $|\hat{\mathbf{y}}|_n$ is the magnitude of the n th Fourier mode of \mathbf{y} minus its mean. Large changes in the dynamics are most likely to occur within time intervals of length equal to the largest Fourier mode. We let $\rho := \|\phi'_k\|_\infty / \|\phi_k\|_\infty$ which selects the polynomial degree p as follows. Analytically,

$$\rho = \frac{2\sqrt{2p-1}}{b-a} \left(\frac{1-1/p}{1-1/2p} \right)^{p-1} = \frac{1.67 \dots}{b-a} \left(p^{1/2} + p^{-1/2} \right) + o(p^{-1/2})$$

and so we set $p = \lceil \rho^2 \frac{|b-a|^2}{2.8} \rceil$. The shift parameter $s \in [0, 1]$ is then used to determine K and the endpoints $[a_k, b_k]$:

$$s = \phi_k(t^*) = \phi_{k+1}(t^*),$$

in other words s is the height of intersection between ϕ_k and ϕ_{k+1} . This fixes $a_{k+1} - a_k = \Delta t L \sqrt{1 - s^{1/p}}$ for each pair of neighboring test functions and measures the amount of overlap between successive test functions, which factors into the covariance matrix Ω . Larger s implies that neighboring basis functions overlap on more points, with $s = 1$ indicating that $\phi_k = \phi_{k+1}$. Specifically, neighboring basis functions overlap on $\lfloor L(1 - \sqrt{1 - s^{1/p}}) \rfloor$ timepoints.

In Figures 3 and 4 we vary the parameters ρ and s and observe that results agree with intuition: larger ρ and smaller s lead to better recovery of \mathbf{w}^* .

$\hat{\mathbf{w}} = \mathbf{Weak_SINDy_UG}(\mathbf{y}, \mathbf{t} ; (f_j)_{j \in [J]}, \rho, s, \lambda, \gamma)$:

- (1) Construct matrix of trial gridfunctions $\Theta(\mathbf{y}) = [f_1(\mathbf{t}, \mathbf{y}) \mid \dots \mid f_J(\mathbf{t}, \mathbf{y})]$
- (2) Construct integration matrices \mathbf{V}, \mathbf{V}' from test functions $(\phi_k)_{k \in [K]}$ parametrized according to ρ, s and (2.8).
- (3) Compute Gram matrix $\mathbf{G} = \mathbf{V}\Theta(\mathbf{y})$ and right-hand side $\mathbf{b} = -\mathbf{V}'\mathbf{y}$ so that $\mathbf{G}_{kj} = \langle \phi_k, f_j(\mathbf{y}) \rangle$ and $\mathbf{b}_{kd} = -\langle \phi'_k, \mathbf{y}_d \rangle$
- (4) Compute approximate covariance and Cholesky factorization $\Omega = \mathbf{V}'(\mathbf{V}')^T = \mathbf{C}\mathbf{C}^T$
- (5) Solve the ℓ_2 -regularized weighted least-squares problem

$$\hat{\mathbf{w}} = \operatorname{argmin}_{\mathbf{w}} \left\{ (\mathbf{G}\mathbf{w} - \mathbf{b})^T \Omega^{-1} (\mathbf{G}\mathbf{w} - \mathbf{b}) + \gamma^2 \|\mathbf{w}\|_2^2 \right\},$$

using SINDy(λ) to enforce sparsity and Ω^{-1} applied using \mathbf{C} .

Strategy 2: Adaptive Grid. Motivated by the arguments above, we now introduce an algorithm for constructing a test function basis localized near points of large change in the dynamics. This occurs in 3 steps: (1) construct a weak approximation to the derivative of the dynamics $\mathbf{v} \approx \dot{\mathbf{x}}$, (2) sample K points \mathbf{c} from a cumulative distribution ψ with density proportional to the total variation $|\mathbf{v}|$, (3) construct test functions centered at \mathbf{c} using a width-at-half-max parameter r_{whm} . Each of these steps is numerically stable and carried out independently along each dimension. A visual diagram is provided in Figure 1.

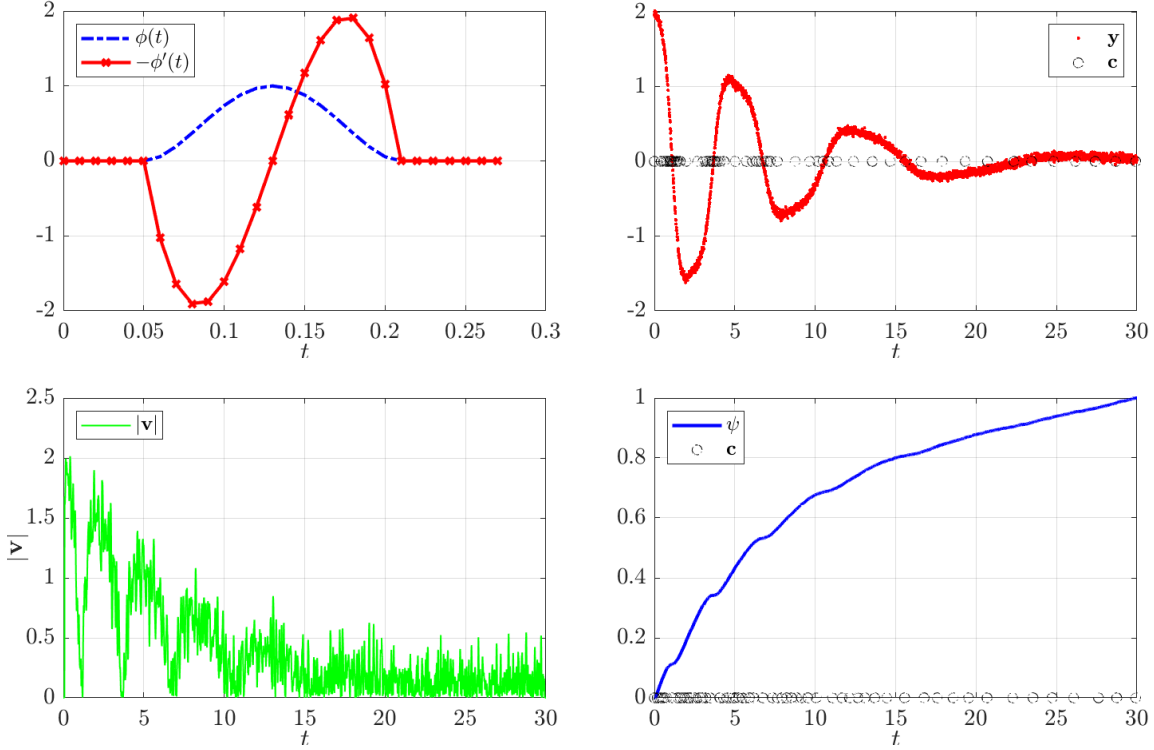


FIGURE 1. Counter-clockwise from top left: test function ϕ and derivative $-\phi'$ used to compute \mathbf{v} , approximate total variation $|\mathbf{v}|$, cumulative distribution $\psi = \int^t |\mathbf{v}| dt$, noisy data \mathbf{y} from the Duffing equation and resulting test functions centers \mathbf{c} .

Step 1: Weak Derivative Approximation: Define $\mathbf{v} := -\mathbf{V}'_p \mathbf{y}$, where the matrix $-\mathbf{V}'_p$ enacts a linear convolution with the derivative of a piece-wise polynomial test function $\phi \in \mathcal{S}$ of degree p and support size s so that

$$\mathbf{v}_m = -\langle \phi', \mathbf{y} \rangle = \langle \phi, \dot{\mathbf{y}} \rangle \approx \dot{\mathbf{y}}_m.$$

The parameters s and p are chosen by the user, with $s = 4$ and $p \geq 2$ corresponding to taking a centered finite difference derivative with 3-point stencil. Larger s results in more smoothing and minimizes the corruption from noise while still capturing the correct large deviations in the dynamics. For all examples we let $p = 2$ and $s = 16$ and note that greater disparity between p and s results in more pronounced localization (less

uniform distribution).

Step 2: Selecting \mathbf{c} : Having computed \mathbf{v} , define ψ to be the cumulative sum of $|\mathbf{v}|$ normalized so that $\max \psi = 1$. In this way ψ is a valid cumulative distribution function with density proportional to the total variation of \mathbf{y} . We then find \mathbf{c} by sampling from ψ . Let $U = [0, \frac{1}{K}, \frac{2}{K}, \dots, 1]$ with K begin the size of the test function basis, we then define $\mathbf{c} = \psi^{-1}(U_k)$, or numerically,

$$\mathbf{c} = \min\{t \in \mathbf{t} : \psi(t) \geq U_k\}.$$

This stage requires the use to select the number of test functions K .

Step 3: Construction of Test functions $(\phi_k)_{k \in [K]}$: Having chosen the location c_k of the centerpoint for each test function ϕ_k , we are left to choose the degree p_k of the polynomial and the supports $[a_k, b_k]$. The degree is chosen according to the width-at-half-max parameter r_{whm} , which specifies the difference in timepoints between each center \mathbf{c}_k and $\arg\{\phi_k(t) = 1/2\}$, while the supports are chosen such that $\phi_k(b_k - \Delta t) = 10^{-16}$. This gives us a nonlinear system of two equations in two unknowns which can be easily solved (i.e. using MATLAB's `fzero`). This can be done for one reference test functions and the rest of the weights obtained by translation.

The adaptive grid Weak SINDy algorithm is summarized as follows:

$\hat{\mathbf{w}} = \mathbf{Weak_SINDy_AG}(\mathbf{y}, \mathbf{t} ; (f_j)_{j \in [J]}, p, s, r_{whm}, K, \lambda, \gamma)$:

- (1) Construct matrix of trial gridfunctions $\Theta(\mathbf{y}) = [f_1(\mathbf{t}, \mathbf{y}) | \dots | f_J(\mathbf{t}, \mathbf{y})]$
- (2) Construct integration matrices \mathbf{V}, \mathbf{V}' from test functions ϕ_k determined adaptively by $\{p, s, r_{whm}, K\}$ according to the procedure above.
- (3) Compute Gram matrix $\mathbf{G} = \mathbf{V}\Theta(\mathbf{y})$ and right-hand side $\mathbf{b} = -\mathbf{V}'\mathbf{y}$ so that $\mathbf{G}_{kj} = \langle \phi_k, f_j(\mathbf{y}) \rangle$ and $\mathbf{b}_{kd} = -\langle \phi'_k, \mathbf{y}_d \rangle$
- (4) Compute approximate covariance and Cholesky factorization $\Omega = \mathbf{V}'(\mathbf{V}')^T = \mathbf{C}\mathbf{C}^T$
- (5) Solve the ℓ_2 -regularized weighted least-squares problem

$$\hat{\mathbf{w}} = \operatorname{argmin}_{\mathbf{w}} \left\{ (\mathbf{G}\mathbf{w} - \mathbf{b})^T \Omega^{-1} (\mathbf{G}\mathbf{w} - \mathbf{b}) + \gamma^2 \|\mathbf{w}\|_2^2 \right\},$$

using SINDy(λ) to enforce sparsity and Ω^{-1} applied using \mathbf{C} .

The parameters p and s play a role in determining how localized the test function basis is around steep gradients and ultimately depend on the timestep Δt . As mentioned above, we set $p = 2$ and $s = 16$ throughout as this produces sufficient localization for the example featured in this article. For simplicity we fix the number of test functions K to be a multiple of the number of trial functions (i.e. $K = J, 2J, 3J$ etc.). For larger noise it is necessary to use a larger basis, while for small noise it is often sufficient to set $K = J$. The optimal value of r_{whm} depends on the timescales of the dynamics and can be chosen from the data using the Fourier transform as in the uniform grid case, however for simplicity we set $r_{whm} = 30$ throughout.

3. NUMERICAL EXPERIMENTS

We now show that the Weak SINDy approach recovers the correct dynamics to high accuracy over a range of signal-to-noise ratios. To generate exact data we use MATLAB's `ode45` with absolute and relative tolerance $1e-10$. Noise is then added to the exact trajectories by fixing σ_{SNR} and adding i.i.d Gaussian noise to each data point with mean zero and variance σ^2 is computed by

$$\sigma = \sigma_{SNR} \|\mathbf{x}\|_{RMS} \quad \text{where} \quad \|\mathbf{x}\|_{RMS} = \sqrt{\frac{1}{DM} \sum_{d=1}^D \sum_{m=1}^M |\mathbf{x}_d(t_m)|^2}.$$

We examine the following canonical nonlinear systems with variations in the specified parameters:

Duffing	$\begin{cases} \dot{x}_1 = x_2, \\ \dot{x}_2 = -\mu x_2 - \alpha x_1 - \beta x_1^3, \end{cases}$	variable β ,	fixed $\mu = 0.2, \alpha = 0.05, \mathbf{x}(0) = \begin{bmatrix} 0 \\ 2 \end{bmatrix}$
Van der Pol	$\begin{cases} \dot{x}_1 = x_2, \\ \dot{x}_2 = \beta x_2(1 - x_1^2) - x_1, \end{cases}$	variable β ,	fixed $\mathbf{x}(0) = \begin{bmatrix} 0 \\ 1 \end{bmatrix}$
Lotka-Volterra	$\begin{cases} \dot{x}_1 = \alpha x_1 - \beta x_1 x_2, \\ \dot{x}_2 = \beta x_1 x_2 - 2\alpha x_2, \end{cases}$	variable β ,	fixed $\alpha = 1, \mathbf{x}(0) = \begin{bmatrix} 1 \\ 2 \end{bmatrix}$
Lorenz	$\begin{cases} \dot{x}_1 = \sigma(x_2 - x_1), \\ \dot{x}_2 = x_1(\rho - x_3) - x_2, \\ \dot{x}_3 = x_1 x_2 - \beta x_3, \end{cases}$	variable $\mathbf{x}(0)$,	fixed $\sigma = 10, \beta = 8/3, \rho = 28$

The Duffing equation and Van der Pol oscillator present cases of an approximately linear systems with cubic nonlinearities. Solutions to the Van der Pol oscillator and Lotka-Volterra system exhibit orbits with variable speed of motion, in particular regions with rapid change between regions of very little variation. For the Lorenz system, we focus on recovering the system in the chaotic regime. For this reason we fix the parameters of the differential equation to lie in the region with large Lyapunov exponents and vary the initial conditions. The initial conditions are chosen from a uniform distribution, $x_1, x_2 \sim U_{[-15, 15]}$ and $x_3 \sim U_{[10, 40]}$, which covers the strange attractor. In this case we see that if the initial conditions lead to trajectories which do not visit both sides of the strange attractor, then the system is not properly identified. This can be expected for recovery in general: trajectories that do not sample important regions of phase space cannot be relied upon to provide an accurate representation of the dynamics at large.

In what follows the sparsity and regularization parameters are set to $\lambda = \frac{1}{4} \min_{\mathbf{w}^* \neq 0} |\mathbf{w}^*|$ and $\gamma = 0$.

3.1. Noise-Free Data (Figure 2). Here we show that in the zero-noise case ($\epsilon = 0$) we recover the correct weight matrix \mathbf{w}^* to within the tolerance of the ODE solver, which is fixed at 10^{-10} . We find that accurate recovery occurs regardless of sparsity enforcement or regularization, and so we set $\lambda = 0.001$, orders of magnitude below any of the coefficients, and $\gamma = 0$. For the data-driven trial basis $(f_j)_{j \in [J]}$, we include all polynomials up to degree 5 in the state variables as well as $\cos(nx_i)$, $\sin(nx_i)$ for $n = 1, 2$ and i ranging

from 1 to D . In addition, we find that recovery occurs with the minimal number of basis functions $K = J$, making the Gram matrix G square. We use the uniform grid approach above with support L selected from the Fourier transform of \mathbf{y} and shift parameter s fixed to ensure that $K = J$.

The main goal of these figures is to examine the effect of increasing the polynomial degree p of the test functions to show that convergence to machine precision is realized in this limit (i.e. convergence to within the accuracy tolerance of the ODE solver). The only outlier in this regard is the Lorenz equation, where for some trajectories the system is not recovered. We find that recovery fails precisely for trajectories that do not visit both sides of the Lorenz attractor, and so inaccurate recovery can be attributed to not have visited a significant enough region of phase space.

3.2. Small-Noise Regime (Figures 3 and 4). We now turn to the case of low to moderate noise levels, examining a signal-to-noise ratio σ_{SNR} in the range $[10^{-5}, 0.04]$. We observe another nice property of the Weak SINDy method, that the error in the coefficients scales with σ_{SNR} , in that the recovered coefficients $\hat{\mathbf{w}}$ having approximately $\log_{10}(10\sigma_{SNR}^{-1})$ significant digits.

We again use the uniform grid approach. We examine not only the polynomial degree p but the number of basis functions K used in recovery. To reiterate the arguments above, the magnitude of ϕ'_k compared to ϕ_k affects the distribution of the residual, so we define $\rho := \|\phi'_k\|_\infty / \|\phi_k\|_\infty$ and define the degree p by fixing ρ and then calculating p . In this way, increasing ρ corresponds to increasing p . We look at $\rho \in [1, 5]$ which corresponds roughly to $p \in [4, 100]$. This together with the spacing parameter s determines the test functions basis. We enforce that two neighboring basis functions ϕ_k and ϕ_{k+1} intersect at a height of s , so that with $s = 1$, the two functions perfectly overlap, and with $s = 0$ their supports are disjoint. In this way, larger s corresponds to higher K . We examine $s \in (0, 1)$. For $s = 0.5$ (featured in both Figures) we note that as ρ is varied from 1 to 5, the number of basis functions K ranges from 21 to 105, or $K = J$ to $K = 5J$.

We simulated 200 instantiations of noise for the Duffing equation and Van der Pol oscillator and for each noisy trajectory examined a range of the parameter values s and ρ . As one might expect from the noise-free case above, increasing ρ leads monotonically to better recovery. In addition, increasing s also leads to better recovery. The mean and standard deviation of the coefficient error $\|\hat{\mathbf{w}} - \mathbf{w}^*\|_2 / \|\mathbf{w}^*\|$ are also pictured, along with sample resulting data-driven dynamical systems, with trajectories denoted by \mathbf{x}_{dd} .

3.3. Large-Noise Regime (Figures 5 to 8). For the last set of experiments we show that recovery in the large noise regime is satisfactory using strategy 2 (non-uniform grid). The signal to noise ratio is $\sigma_{SNR} = 0.1$ for the Duffing, Van der Pol and Lorenz equations, and $\sigma_{SNR} = 0.05$ for Lotka-Volterra. In each case we set the weak differentiation parameters to $p = 2$ and $s = 16$ and the width-at-half-max to $r_{whm} = 30$ timepoints. For the 2D systems, we use $K = 6J = 126$ test basis functions, while for the Lorenz equation $K = 4J = 224$ were used. In each case the correct terms were identified with relative ℓ_2 coefficient error less than 10^{-2} , indicating approximately two significant digits. We plot the noisy data \mathbf{y} , the true data \mathbf{x} and the simulated data-driven dynamical systems \mathbf{x}_{dd} in dynamo view and phase space to exemplify the separation of scales

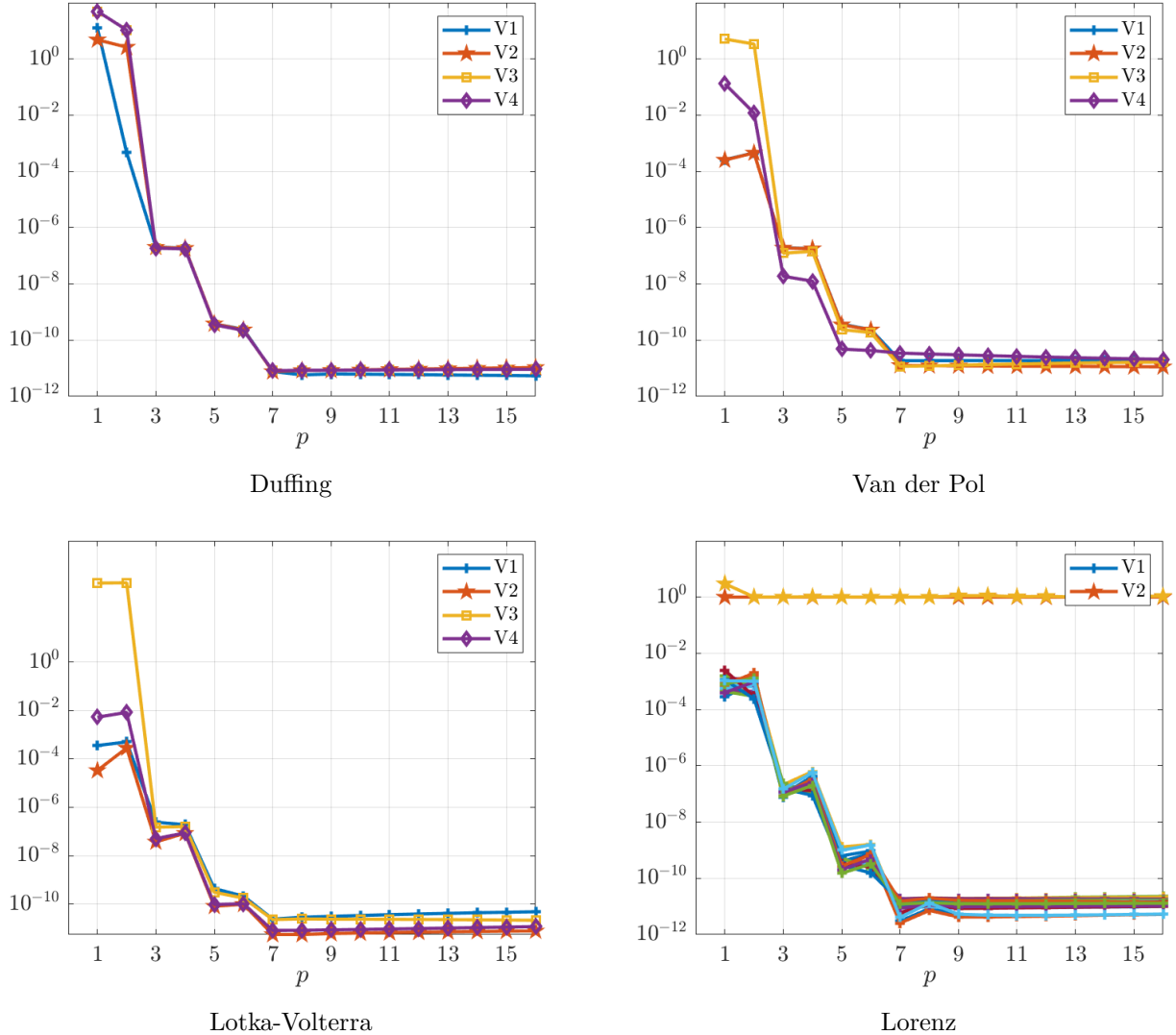


FIGURE 2. Plots of relative error $\|\hat{\mathbf{w}} - \mathbf{w}^*\|_2 / \|\mathbf{w}^*\|_2$ vs. p when $\epsilon = 0$. For each system, a range of parameter values is considered, indicated by the different versions V1-V4. For the Duffing equation, Van der Pol oscillator and Lotka-Volterra system we see convergence in the recovery of coefficients using the uniform-grid Weak SINDy approach (Strategy 1) to the accuracy of the ODE solver (10^{-10}) as p is increased. For the Lorenz system, 20 random initial conditions were selected with 2/20 trajectories not yielding recovery of the correct coefficients due to having not visited both sides of the Lorenz strange attractor.

	V1	V2	V3	V4	Notes
Duffing, β :	0.005	0.08	1	100	$\mathbf{t} = 0 : 0.01 : 30$
Van der Pol, β :	0.01	0.1	1	10	$\mathbf{t} = 0 : 0.01 : 30$
Lotka-Volterra, β :	0.05	0.1	1	10	$\mathbf{t} = 0 : 0.01 : 30$
Lorenz	(see below)	(see below)	-	-	$\mathbf{x}(0) \sim U_{[-15, 15]^2 \times [10, 40]}, \mathbf{t} = (0.005 : 0.005 : 10)$

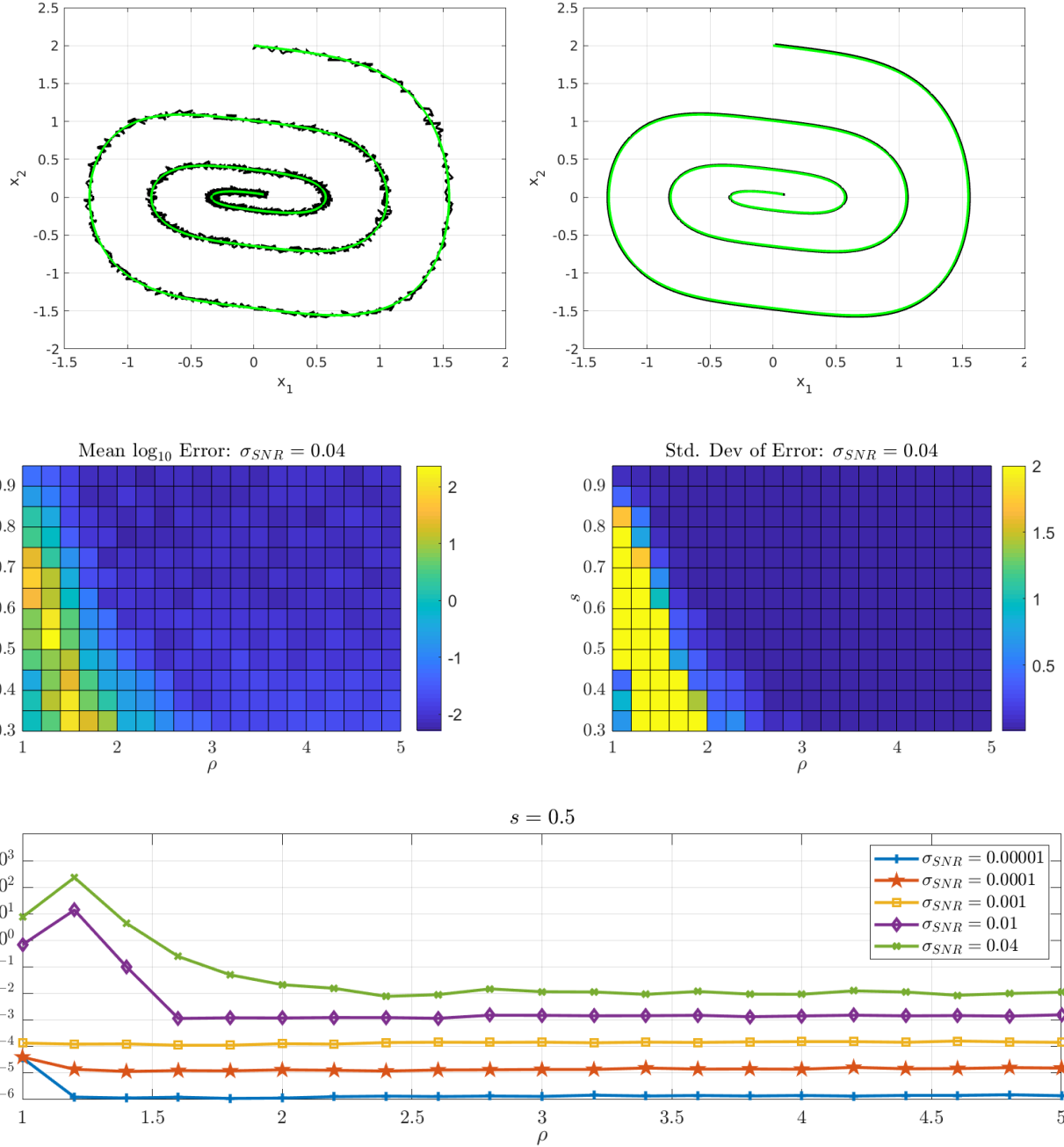


FIGURE 3. Dynamic recovery of the Duffing equation with parameters $\mu = 0.2$, $\alpha = 0.05$, $\beta = 1$. Top row: example trajectory \mathbf{y} (left) and learned dynamics \mathbf{x}_{dd} (right) both plotted over true data \mathbf{x} with $\sigma_{SNR} = 0.04$, $\rho = 5$, $s = 0.5$ and an error of $E := \|\mathbf{w} - \mathbf{w}^*\|_2 / \|\mathbf{w}^*\|_2 = 0.0009$. Middle row: heat map of the \log_{10} average error E (left) and standard deviation (right) over 200 noisy trajectories with $\sigma_{SNR} = 0.04$ with increasing ρ along the x -axis and increasing s along the y -axis. Bottom: decreasing error trend for fixed $s = 0.5$ for various σ_{SNR} . For each σ_{SNR} the expected error falls roughly an order of magnitude below the σ_{SNR} as ρ increases.

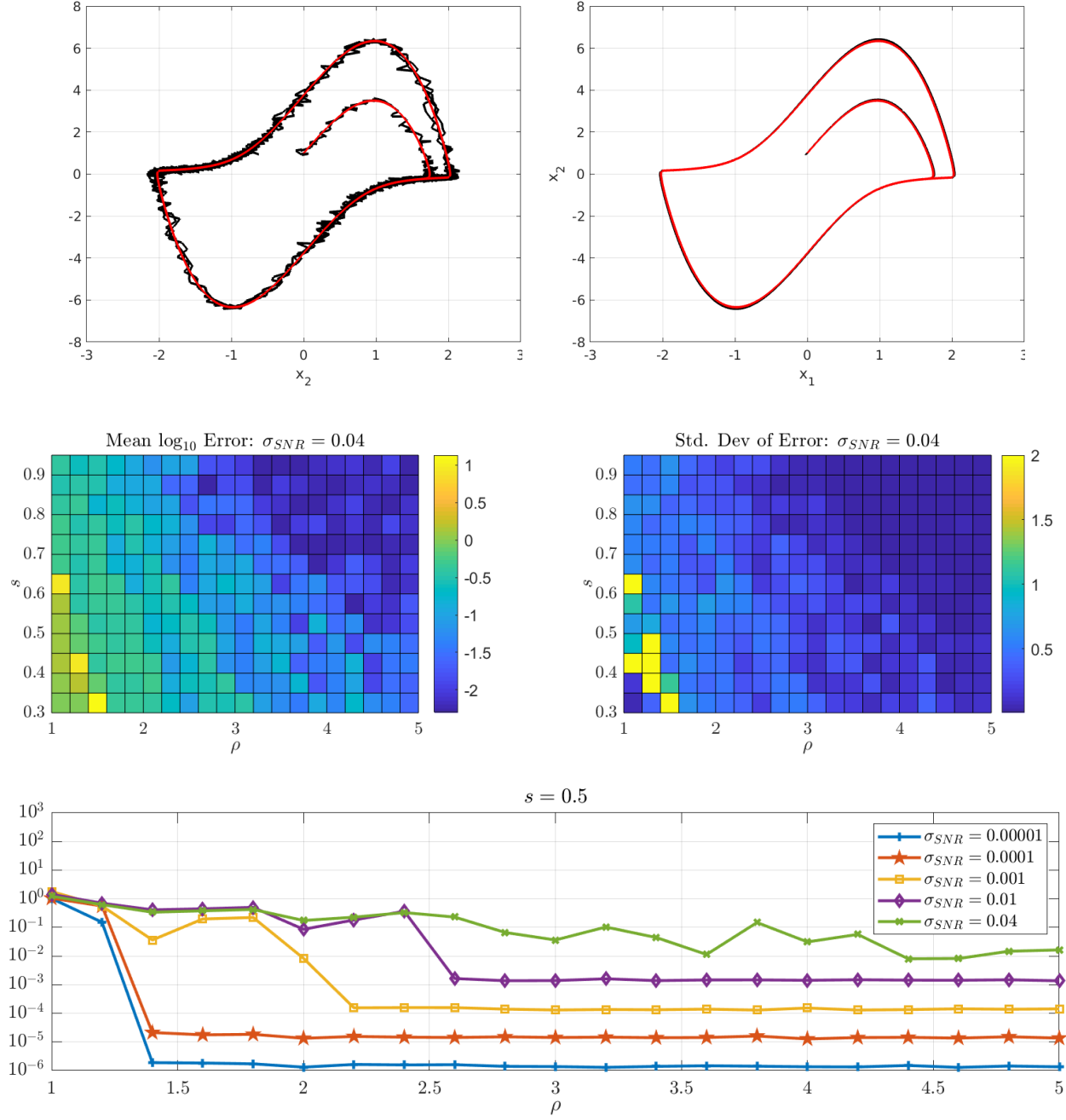


FIGURE 4. Dynamic recovery of the Van der Pol oscillator with parameter $\mu = 4$. Top row: example trajectory \mathbf{y} (left) and learned dynamics \mathbf{x}_{dd} (right) both plotted over true data \mathbf{x} with $\sigma_{SNR} = 0.04$, $\rho = 5$, $s = 0.5$ and an error of $E := \|\hat{\mathbf{w}} - \mathbf{w}^*\|_2 / \|\mathbf{w}^*\|_2 = 0.0026$. Middle row: color plot of \log_{10} of the average error E (left) and standard deviation of the error E (right) over 200 noisy trajectories with $\sigma_{SNR} = 0.04$ with increasing ρ along the x -axis and increasing s along the y -axis. Bottom: decreasing error trend for fixed $s = 0.5$ for various σ_{SNR} . As with the Duffing equation in Figure 3, for each σ_{SNR} the expected error falls roughly an order of magnitude below the σ_{SNR} as ρ increases, however the expected accuracy begins to break down for larger σ_{SNR} , motivating Strategy 2.

and the severity of the corruption from noise. We extend \mathbf{x}_{dd} by 50%.

For the Duffing equation, the data-driven trajectory \mathbf{x}_{dd} diverges slightly from the true data as the system relaxes to equilibrium but is otherwise qualitatively accurate. The Van der Pol oscillator exhibits a case of nearly the same limit cycle being identified but the dominant timescale of \mathbf{x}_{dd} is slightly different than that of \mathbf{x} , so that the data-driven trajectories diverge over time while visiting the same region of phase space. This suggests the level of accuracy needed to accurately recover systems from trajectories with sharp gradients. The recovered Lotka-Volterra trajectory is nearly indistinguishable from the true data. The recovered Lorenz trajectory remains close to the true trajectory up until around $t = 3$, before the two diverge as is expected from chaotic dynamics. The Lorenz attractor is captured.

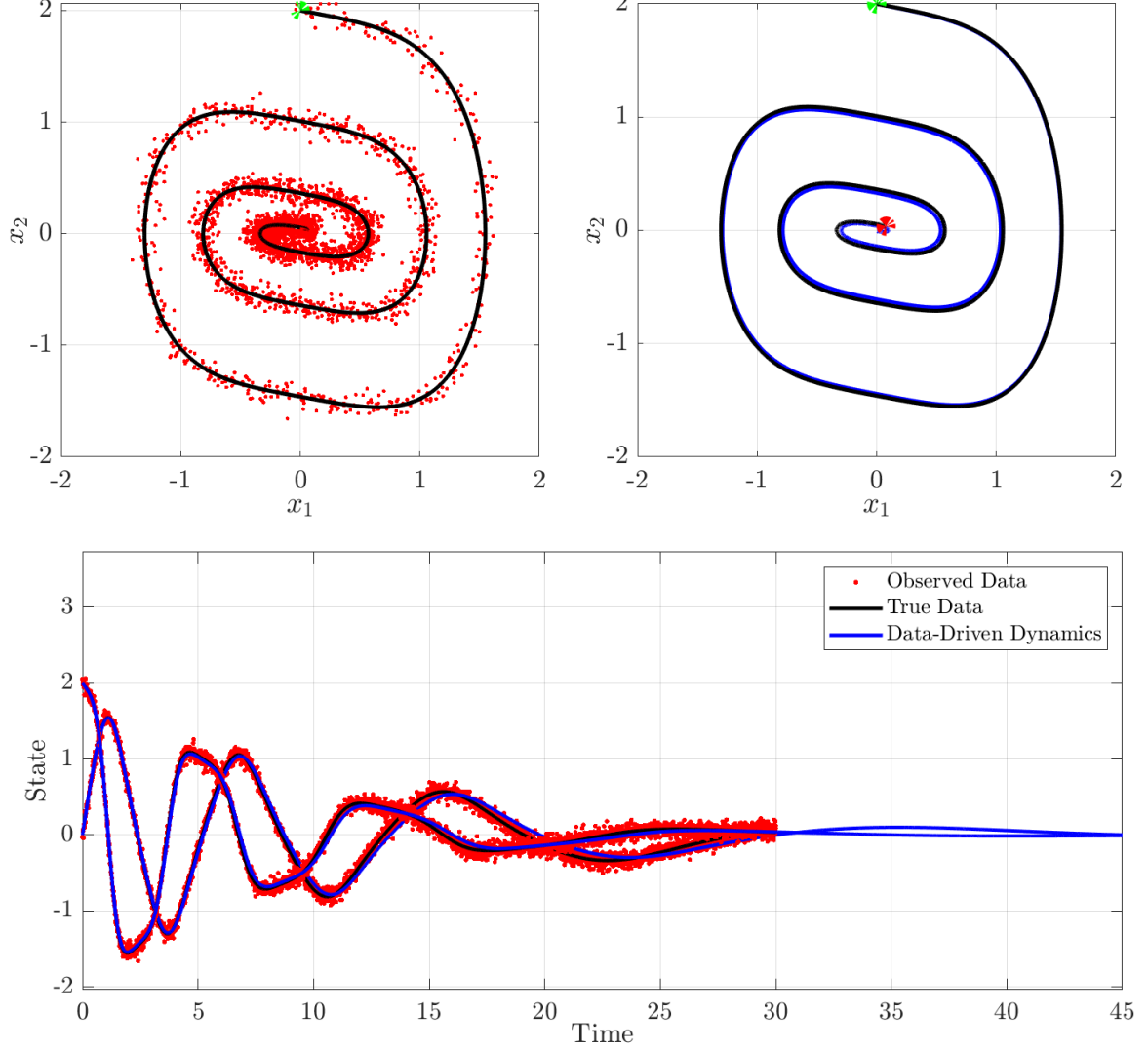


FIGURE 5. Duffing Equation, same parameters as in Figure 3. Accurate recovery of the stable spiral with $\sigma_{SNR} = 0.1$. All correct terms were identified with an error in the weights of $\|\hat{\mathbf{w}} - \mathbf{w}^*\|_2 / \|\mathbf{w}^*\|_2 = 0.007$ and $\|\mathbf{x}_d - \mathbf{x}\|_2 / \|\mathbf{x}\|_2 = 0.097$. The number of basis functions used was $K = 6J = 126$ and the width-at-half-max parameter was set to $r_{whm} = 30$ time-points, resulting in $p = 10$.

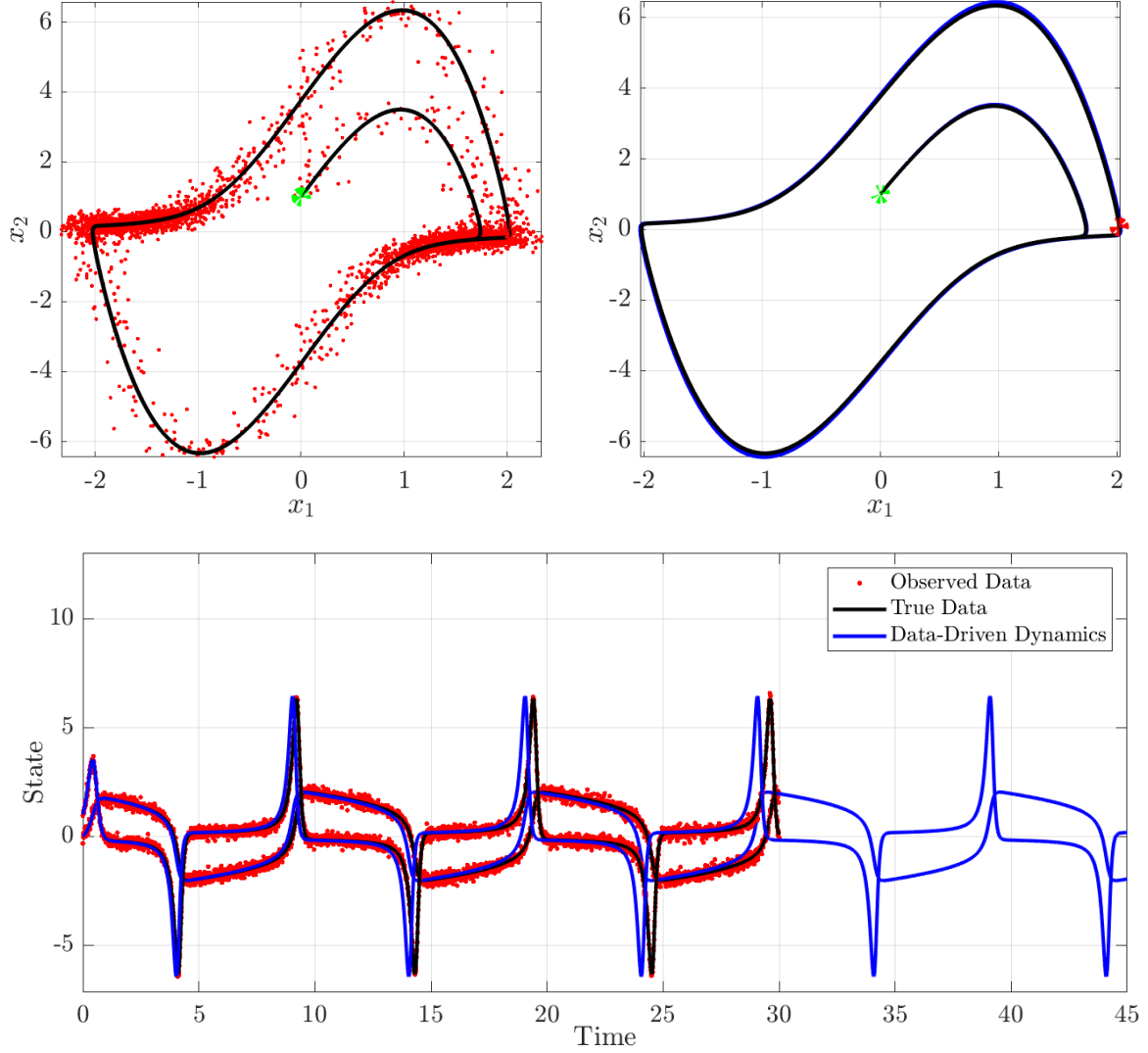


FIGURE 6. Van der Pol oscillator, same parameters as in Figure 4. Accurate recovery of the limit cycle for $\sigma_{SNR} = 0.1$. All correct terms were identified with an error in the weights of $\|\hat{\mathbf{w}} - \mathbf{w}^*\|_2 / \|\mathbf{w}^*\|_2 = 0.008$ and $\|\mathbf{x}_d - \mathbf{x}\|_2 / \|\mathbf{x}\|_2 = 0.56$. The number of basis functions used was $K = 6J = 126$ and the width-at-half-max parameter was set to $r_{whm} = 30$ timepoints, resulting in $p = 10$. Here we see that the data-driven system \mathbf{x}_{dd} traverses the limit cycle with a slightly longer period, resulting in a growing pointwise error between the \mathbf{x}_{dd} and the true state \mathbf{x} .

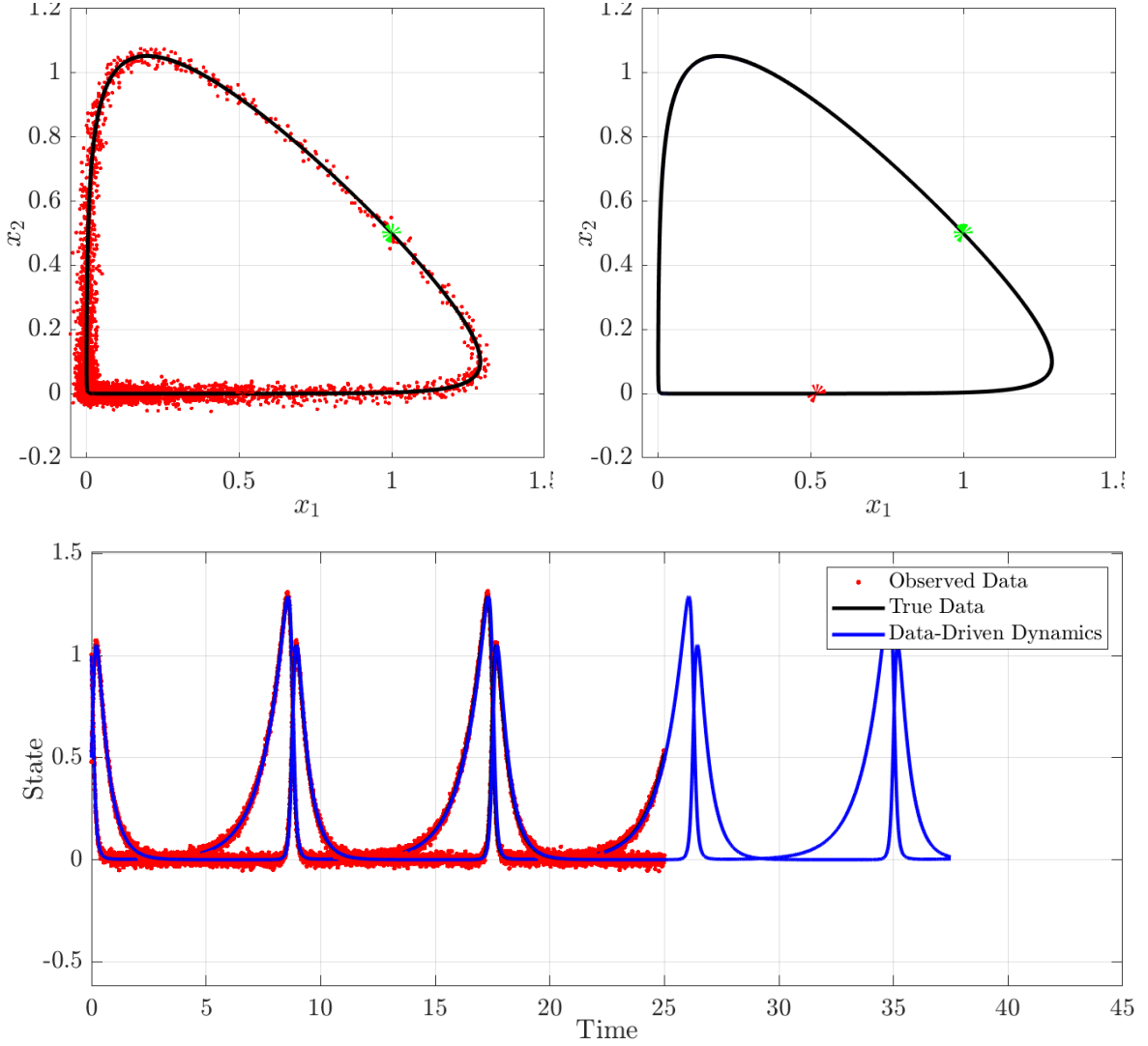


FIGURE 7. Lotka-Volterra system with $\alpha = 1, \beta = 10$. Accurate recovery of the limit cycle for $\sigma_{SNR} = 0.05$. All correct terms were identified with an error in the weights of $\|\hat{\mathbf{w}} - \mathbf{w}^*\|_2 / \|\mathbf{w}^*\|_2 = 0.0032$ and $\|\mathbf{x}_d - \mathbf{x}\|_2 / \|\mathbf{x}\|_2 = 0.065$. The number of basis functions used was $K = 6J = 126$ and the width-at-half-max parameter was set to $r_{whm} = 30$ timepoints, resulting in $p = 10$. The data-driven system \mathbf{x}_{dd} accurately captures the limit cycle and traverses at the same speed as the true data \mathbf{x} . Here we set $\gamma = 0.01$ and normalized the columns of $\Theta(\mathbf{y})$ using the 2-norm as the original system is nearly linearly dependent.

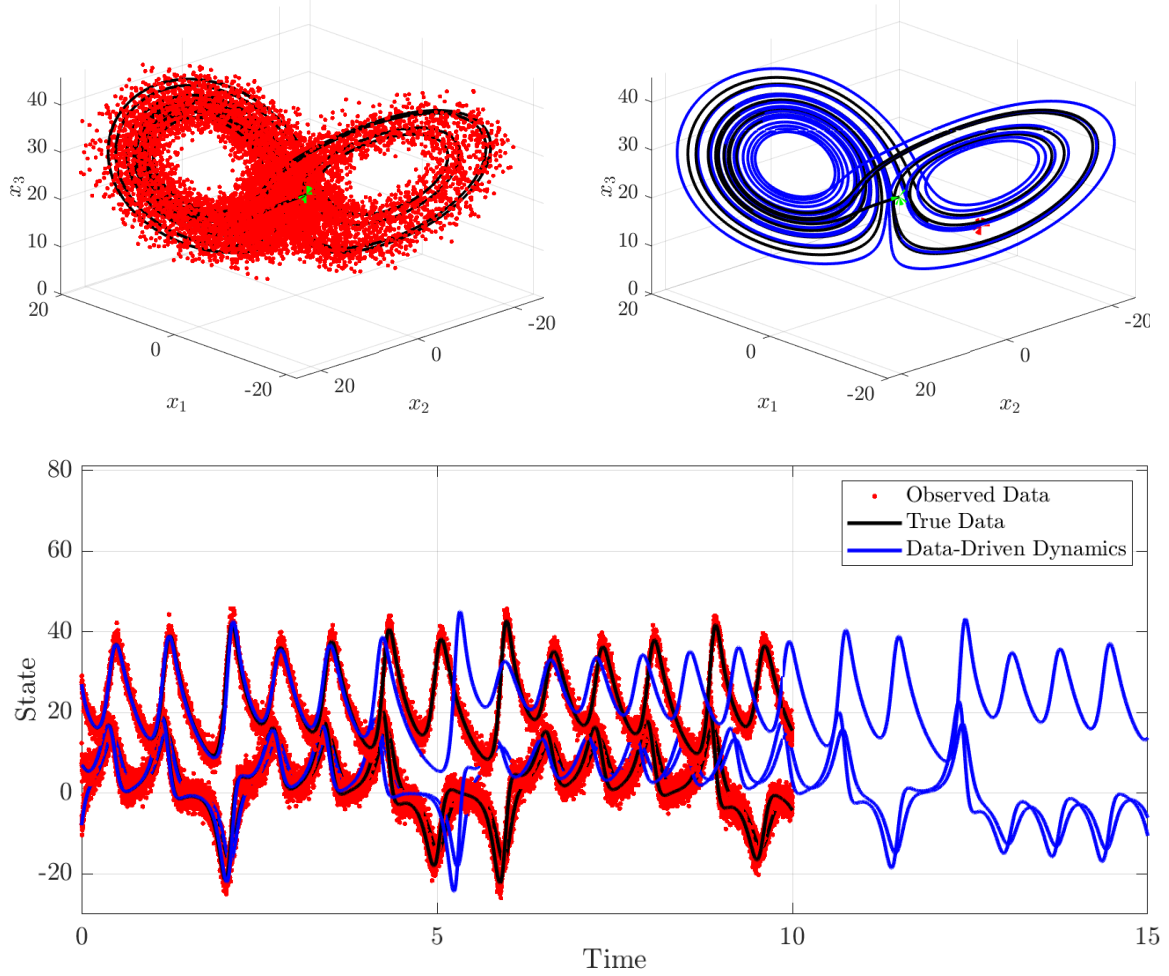


FIGURE 8. Lorenz system with $\mathbf{x}_0 = [-8 \ 7 \ 27]^T$. Accurate recovery of the strange attractor for $\sigma_{SNR} = 0.1$. All correct terms were identified with an error in the weights of $\|\hat{\mathbf{w}} - \mathbf{w}^*\|_2 / \|\mathbf{w}^*\|_2 = 0.0091$. Since the system is chaotic it does not make sense to measure the pointwise error between the data-driven trajectory \mathbf{x}_{dd} and the true data \mathbf{x} for large times, but using data up until $t = 3$ (first 3000 timepoints) we can report a reasonable pointwise agreement of $\|\mathbf{x}_d - \mathbf{x}\|_2 / \|\mathbf{x}\|_2 = 0.047$. The number of basis functions used was $K = 4J = 224$ and the width-at-half-max parameter was set to $r_{whm} = 30$ timepoints, resulting in $p = 10$.

4. CONCLUSION

We have developed and investigated a data-driven model selection algorithm based on the weak formulation of differential equations. The algorithm utilizes the linear formulation of the model selection problem in terms of solving for weights \mathbf{w} of a candidate function basis $(f_j)_{j \in [J]}$ introduced in [7] and expanded upon in [1]. Our Weak SINDy algorithm can be seen as a generalization of the sparse recovery using integral terms found in [6], where dynamics were recovered from the integral equation. For future work, we aim to improve upon

this method by incorporating more information about the model selection framework into the error structure of the residuals and adapting the current framework to handle multiple scales and spatiotemporal data.

REFERENCES

- [1] Steven L Brunton, Joshua L Proctor, and J Nathan Kutz. Discovering governing equations from data by sparse identification of nonlinear dynamical systems. *Proceedings of the national academy of sciences*, 113(15):3932–3937, 2016.
- [2] Sung Ha Kang, Wenjing Liao, and Yingjie Liu. Ident: Identifying differential equations with numerical time evolution. *arXiv preprint arXiv:1904.03538*, 2019.
- [3] Rachel Keller and Qiang Du. Discovery of dynamics using linear multistep methods. *arXiv preprint arXiv:1912.12728*, 2019.
- [4] Samuel H Rudy, Steven L Brunton, Joshua L Proctor, and J Nathan Kutz. Data-driven discovery of partial differential equations. *Science Advances*, 3(4):e1602614, 2017.
- [5] Samuel H Rudy, J Nathan Kutz, and Steven L Brunton. Deep learning of dynamics and signal-noise decomposition with time-stepping constraints. *Journal of Computational Physics*, 396:483–506, 2019.
- [6] Hayden Schaeffer and Scott G McCalla. Sparse model selection via integral terms. *Physical Review E*, 96(2):023302, 2017.
- [7] Wen-Xu Wang, Rui Yang, Ying-Cheng Lai, Vassilios Kovanis, and Celso Grebogi. Predicting catastrophes in nonlinear dynamical systems by compressive sensing. *Physical review letters*, 106(15):154101, 2011.
- [8] Linan Zhang and Hayden Schaeffer. On the convergence of the sindy algorithm. *Multiscale Modeling & Simulation*, 17(3):948–972, 2019.
- [9] Sheng Zhang and Guang Lin. Robust data-driven discovery of governing physical laws with error bars. *Proceedings of the Royal Society A: Mathematical, Physical and Engineering Sciences*, 474(2217):20180305, 2018.
- [10] Sheng Zhang and Guang Lin. Robust subsampling-based sparse bayesian inference to tackle four challenges (large noise, outliers, data integration, and extrapolation) in the discovery of physical laws from. *arXiv preprint arXiv:1907.07788*, 2019.

E-mail address: daniel.messenger@colorado.edu¹

¹Department of Applied Mathematics, University of Colorado Boulder, 11 Engineering Dr., Boulder, CO 80309, USA.